

# Online Research @ Cardiff

This is an Open Access document downloaded from ORCA, Cardiff University's institutional repository: <https://orca.cardiff.ac.uk/id/eprint/89712/>

This is the author's version of a work that was submitted to / accepted for publication.

Citation for final published version:

You, Jong-Burn, Lee, Wook-Jae ORCID: <https://orcid.org/0000-0001-8430-4797>, Won, Dongshik and Yu, Kyoungsik 2014. Multiband perfect absorbers using metal-dielectric films with optically dense medium for angle and polarization insensitive operation. Optics Express 22 (7) , pp. 8339-8348. 10.1364/OE.22.008339 file

Publishers page: <http://dx.doi.org/10.1364/OE.22.008339>  
<<http://dx.doi.org/10.1364/OE.22.008339>>

Please note:

Changes made as a result of publishing processes such as copy-editing, formatting and page numbers may not be reflected in this version. For the definitive version of this publication, please refer to the published source. You are advised to consult the publisher's version if you wish to cite this paper.

This version is being made available in accordance with publisher policies.

See

<http://orca.cf.ac.uk/policies.html> for usage policies. Copyright and moral rights for publications made available in ORCA are retained by the copyright holders.



# Multiband perfect absorbers using metal-dielectric films with optically dense medium for angle and polarization insensitive operation

Jong-Bum You,<sup>1</sup> Wook-Jae Lee,<sup>1,2</sup> Dongshik Won,<sup>1</sup> and Kyoungsik Yu<sup>1,\*</sup>

<sup>1</sup>Department of Electrical Engineering, KAIST, Daejeon, South Korea

<sup>2</sup>Currently with Department of Electrical and Computer Engineering, University of California, Davis, California, USA

\*ksyu@kaist.edu

**Abstract:** The cavity resonant properties of planar metal-dielectric layered structures with optically dense dielectric media are studied with the aim of realizing omnidirectional and polarization-insensitive operation. The angle-dependent coupling between free-space and cavity modes are revealed to be a key leverage factor in realizing nearly perfect absorbers well-matched to a wide range of incidence angles. We establish comprehensive analyses of the relationship between the structural and optical properties by means of theoretical modeling with numerical simulation results. The presented work is expected to provide a simple and cost-effective solution for light absorption and detection applications that exploit planar metal-dielectric optical devices.

©2014 Optical Society of America

**OCIS codes:** (230.4170) Multilayers; (230.5750) Resonators; (310.3915) Metallic, opaque, and absorbing coatings; (310.4165) Multilayer design.

---

## References and links

1. M. Scalora, M. J. Bloemer, A. S. Pethel, J. P. Dowling, C. M. Bowden, and A. S. Manka, "Transparent, metallo-dielectric, one-dimensional, photonic band-gap structures," *J. Appl. Phys.* **83**(5), 2377 (1998).
2. K. Aydin, V. E. Ferry, R. M. Briggs, and H. A. Atwater, "Broadband polarization-independent resonant light absorption using ultrathin plasmonic super absorbers," *Nat Commun* **2**, 517 (2011).
3. Y. Q. Ye, Y. Jin, and S. He, "Omnidirectional, polarization-insensitive and broadband thin absorber in the terahertz regime," *J. Opt. Soc. Am. B* **27**(3), 498–504 (2010).
4. X. Liu, T. Starr, A. F. Starr, and W. J. Padilla, "Infrared spatial and frequency selective metamaterial with near-unity absorbance," *Phys. Rev. Lett.* **104**(20), 207403 (2010).
5. S. Shu, Z. Li, and Y. Y. Li, "Triple-layer Fabry-Perot absorber with near-perfect absorption in visible and near-infrared regime," *Opt. Express* **21**(21), 25307–25315 (2013).
6. M. A. Kats, D. Sharma, J. Lin, P. Genevet, R. Blanchard, Z. Yang, M. M. Qazilbash, D. Basov, S. Ramanathan, and F. Capasso, "Ultra-thin perfect absorber employing a tunable phase change material," *Appl. Phys. Lett.* **101**(22), 221101 (2012).
7. D. Y. Lei and H. C. Ong, "Enhanced forward emission from ZnO via surface plasmons," *Appl. Phys. Lett.* **91**(21), 211107 (2007).
8. F. Guo, B. Yang, Y. Yuan, Z. Xiao, Q. Dong, Y. Bi, and J. Huang, "A nanocomposite ultraviolet photodetector based on interfacial trap-controlled charge injection," *Nat. Nanotechnol.* **7**(12), 798–802 (2012).
9. H. A. Atwater and A. Polman, "Plasmonics for improved photovoltaic devices," *Nat. Mater.* **9**(3), 205–213 (2010).
10. M. A. Kats, R. Blanchard, P. Genevet, and F. Capasso, "Nanometre optical coatings based on strong interference effects in highly absorbing media," *Nat. Mater.* **12**(1), 20–24 (2012).
11. H. Shin, M. F. Yanik, S. Fan, R. Zia, and M. L. Brongersma, "Omnidirectional resonance in a metal-dielectric-metal geometry," *Appl. Phys. Lett.* **84**(22), 4421 (2004).
12. J. S. Q. Liu and M. L. Brongersma, "Omnidirectional light emission via surface plasmon polaritons," *Appl. Phys. Lett.* **90**(9), 091116 (2007).
13. A. Hosseini and Y. Massoud, "Optical range microcavities and filters using multiple dielectric layers in metal-insulator-metal structures," *J. Opt. Soc. Am. A* **24**(1), 221–224 (2007).
14. J. Zhang, W. Bai, L. Cai, X. Chen, G. Song, and Q. Gan, "Omnidirectional absorption enhancement in hybrid waveguide-plasmon system," *Appl. Phys. Lett.* **98**(26), 261101 (2011).

15. T. V. Teperik, F. J. García de Abajo, A. G. Borisov, M. Abdelsalam, P. N. Bartlett, Y. Sugawara, and J. J. Baumberg, "Omnidirectional absorption in nanostructured metal surfaces," *Nat. Photonics* **2**(5), 299–301 (2008).
16. P. Bouchon, C. Koechlin, F. Pardo, R. Haïdar, and J.-L. Pelouard, "Wideband omnidirectional infrared absorber with a patchwork of plasmonic nanoantennas," *Opt. Lett.* **37**(6), 1038–1040 (2012).
17. M. Pu, C. Hu, M. Wang, C. Huang, Z. Zhao, C. Wang, Q. Feng, and X. Luo, "Design principles for infrared wide-angle perfect absorber based on plasmonic structure," *Opt. Express* **19**(18), 17413–17420 (2011).
18. W.-J. Lee, J.-B. You, K. Kwon, B. Park, and K. Yu, "Direction-selective emission with small angular divergence from a subwavelength aperture using radiative waveguide modes," *Phys. Rev. B* **87**(12), 125108 (2013).
19. E. D. Palik, *Handbook of Optical Constants of Solids* (Academic, 1985), Vol. 1.
20. M. A. Gilmore and B. L. Johnson, "Forbidden guided-wave plasmon polaritons in coupled thin films," *J. Appl. Phys.* **93**(8), 4497–4504 (2003).
21. H. A. Haus, *Waves and Fields in Optoelectronics* (Prentice-Hall, 1984).
22. T. J. Seok, A. Jamshidi, M. Kim, S. Dhuey, A. Lakhani, H. Choo, P. J. Schuck, S. Cabrini, A. M. Schwartzberg, J. Bokor, E. Yablonovitch, and M. C. Wu, "Radiation engineering of optical antennas for maximum field enhancement," *Nano Lett.* **11**(7), 2606–2610 (2011).
23. M. De Zoysa, T. Asano, K. Mochizuki, A. Oskooi, T. Inoue, and S. Noda, "Conversion of broadband to narrowband thermal emission through energy recycling," *Nat. Photonics* **6**(8), 535–539 (2012).
24. R. A. Soref and B. R. Bennett, "Electrooptical effects in silicon," *IEEE J. Quantum Electron.* **23**(1), 123–129 (1987).

## 1. Introduction

The metal-dielectric (MD) layered structures have been used for highly reflective and transparent coatings in the area of optoelectronic and photonic applications [1]. More recently, much attention has turned toward the understanding of the subwavelength-perforated MD stacks as a means to support the tight localization of light based on surface plasmon polaritons (SPPs) [2] and metamaterial properties [3, 4]. Such versatile optical properties of the MD-layered structures can provide a promising route to manipulate the interaction between light and matter in integrated photonic devices including perfect absorbers [2–6], light-emitting diodes [7], photo-detectors [8], photovoltaic cells [9], and optical filters [10].

Among many features of the MD-layered structures, the omnidirectional resonance (ODR) has been considered as a crucial requirement for a wide acceptance angle in a number of light absorbing and filtering applications [10–13]. Numerous investigations have focused on achieving the ODR in metal-dielectric-metal (MDM) structures by using the radiative SPPs with flat dispersion bands [11–13]. For such operations, the thickness of the dielectric layer  $d$  with permittivity  $\varepsilon$  must be tuned to be equal to  $d \approx \lambda_{sp} / (4\sqrt{\varepsilon})$ , where  $\lambda_{sp}$  is the SPP resonance wavelength [11]. In these regards, the ODR frequency is unique for each dielectric material, thus it is difficult to alter the resonant wavelength. One-dimensional (1D) grating patterns can be used as a solution to provide customization of the spectral response of the MDM structures [14]. Although the tailored multiband absorption can be realized with the one-dimensional grating patterns when compared to the continuous and all-planar MDM structures, these examples are limited to only one input polarization state due to the lack of the rotational symmetry. To facilitate the ODR for both the transverse electric (TE) and transverse magnetic (TM) polarized light, the MDM structures with two-dimensional patterns have been proposed [2, 3, 15–17]. The two-dimensional arrays of cross-shaped and crossed-trapezoidal patterns enable the omnidirectional absorption for both TM and TE polarizations [2, 3]. However, the multi-step fabrication processes with subwavelength-scale feature dimensions require precise manufacturing tolerances and might not be suitable for large-area applications.

The aforementioned techniques mainly rely on the patterned MDM structures or require an optimum dielectric thickness to support a flat band dispersion relationship [11–13]. However, similar results with large acceptance angles and high absorptivities have been recently obtained through only a pair of MD layers by means of ultra-thin optical coatings of a lossy and optically dense material (Germanium) on a metal substrate [10]. Especially, although special optical design schemes for the flat dispersion bands were not used, wide

acceptance angles for both TE and TM polarized light were maintained. More recently, other reports have pointed out that the MDM triple-layer structures can support highly directional angular absorption and emission when employing low refractive index dielectric medium [5, 18]. Based on these findings, we anticipate that the angular responses in the MD-layered structures strongly depend on their core dielectric material properties.

In this paper, we demonstrate the omnidirectional and polarization-insensitive operation of the MDM structures by employing an optically-dense dielectric core layer. The ODR behaviors of cavity resonances are described in terms of the dispersion properties of radiative waveguide modes (RWMs) whose radiated fields are oscillatory in the light incident direction. The RWMs (often referred to as leaky modes in the literature) can be loosely or tightly bound by a partially reflective interface between the free-space and the MD-layered absorbers, and their normalized absorbance can thus be raised up to around 100% under a critical coupling condition where the internal and external losses of the thin film cavity are equal to each other. On the basis of the critical coupling behavior, we demonstrate that the MDM structures can serve as multiband absorbers for almost complete absorption at a wide range of incidence angles irrespective of its polarization state.

## 2. Dispersion relations of the MDM structures

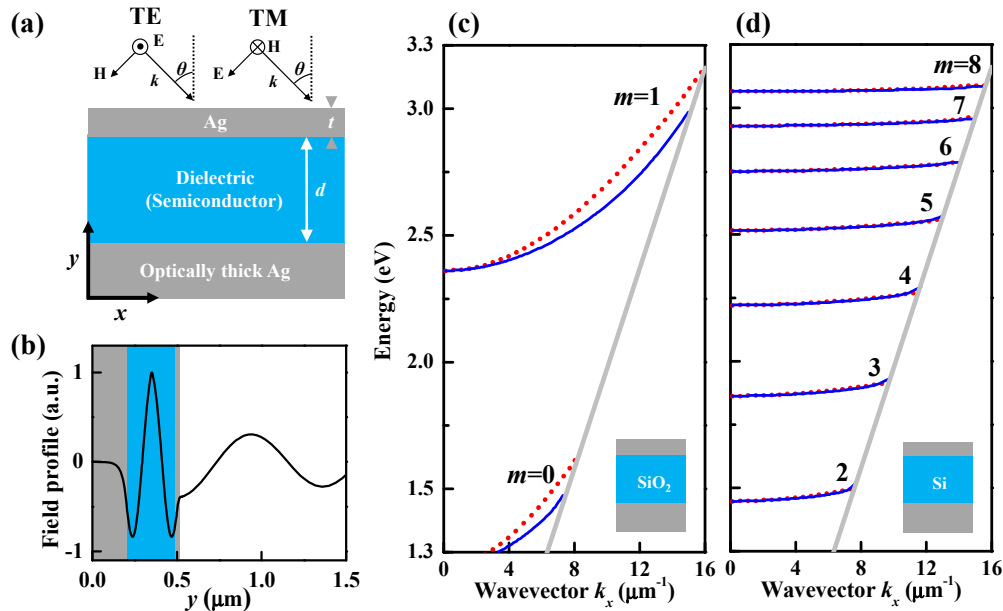


Fig. 1. (a) Schematic description of a metal-dielectric-metal (MDM) structure. The gray and blue regions represent the metal and dielectric layers, respectively. (b) Normalized field profile of the RWMs (two nodes within the dielectric core and thus  $m = 2$ ) of the MDM structure ( $t = 20$  nm,  $d = 300$  nm) with a Si core layer (blue region). The calculated dispersion curves of TM (blue solid lines) and TE (red dotted lines) modes supported by the MDM structure with the core layer material of (c)  $\text{SiO}_2$  and (d) Si are shown.

The dispersion relations for the MDM structure are presented to reveal the role of the material properties on the ODR of the RWMs using the transfer matrix method (TMM) [18]. For our purpose, it is convenient to compare the MDM structures containing a lower- $n$  ( $\text{SiO}_2$ ) and higher- $n$  dielectric (Silicon) core medium. The dispersion curves are computed based on the structural model schematically drawn in Fig. 1(a). The thickness of the core dielectric layer for both cases was chosen to be  $d = 300$  nm for this analysis to enable multiband resonance so that we can analyze the absorption characteristics of multiple modes. The core dielectric layer is covered by a top metal (Ag) layer whose thickness is  $t = 20$  nm and thin enough for easy

optical coupling from the incident beam. The core dielectric layer is placed on top of a 200 nm-thick metal (Ag) bottom layer, which sufficiently blocks the substrate transmission. The complex refractive index data of Ag, Si, and SiO<sub>2</sub> were taken from Palik [19]. We considered the TE (TM) polarized light whose electric field  $E$  (magnetic field  $H$ ) is perpendicular to the plane of the incidence ( $x$ - $y$  plane). As an example, the normalized electric field profile of the second order RWMs is plotted in Fig. 1(b) for the Ag-Si-Ag structure. The number of field nodes at the dielectric core gives the mode order,  $m$ .

Figure 1(c) shows the calculated dispersion curves of the MDM structure with a lower- $n$  dielectric core medium. The incident angle corresponding to the in-plane wavevector  $k_x$  is determined by  $k_x = (2\pi/\lambda)(\sin\theta)$ , where  $\lambda$  represents the peak wavelength. The first order modes ( $m = 1$ ) for each polarization have the identical energy (2.36 eV) at  $k_x = 0$  (normal incidence). As  $k_x$  increases, however, they are significantly bent upward and split into two distinct resonances with different polarizations. When the dispersion curves reach the light-line (highly oblique incidence), the photon energies of TE and TM resonances are blue-shifted differently to be resonant at 3.17 eV and 2.99 eV, respectively. These blue-shifts of resonant peaks are responsible for the highly directional operation [5, 18]. On the other hand, the MDM structure with a higher- $n$  dielectric core layer can realize nearly flat and polarization-independent resonances (Fig. 1(d)). In this case, the photon energies of the RWMs do not change significantly from normal incidence to high-grazing incidence ( $\theta \sim 80^\circ$ ). When the incident angle changes from  $\theta = 0^\circ$  to  $80^\circ$ , negligible frequency shift of 1% (6.4%) is observed for  $m = 8$  ( $m = 2$ ) located in the resonant frequency of around 3.06 eV (1.43 eV).

The reason behind the material-dependent behaviors is associated with the fact that the group velocity decreases more rapidly with the higher- $n$  materials [20]. It should be pointed out that such a dramatic reduction of the group velocity appeared here and for example in [10] can lead to the angle-insensitive absorption. In these regards, the higher-order modes exhibit more omnidirectional resonances since the refractive index  $n$  of Si becomes larger in the shorter wavelength region. The resonant frequency shift from  $\theta = 0^\circ$  to  $80^\circ$  for different resonances with corresponding refractive index ( $n$ ) and extinction coefficient ( $k$ ) of Si from [19] are summarized in Table 1. Multiple resonances with a shorter free-spectral-range appear for the higher- $n$  core medium due to the increase in the effective optical path length. The resonant frequencies and the absorptivities of such modes can be fine-tuned by changing  $d$  and  $t$ , respectively, while maintaining a polarization-insensitive ODR.

**Table 1. ODR frequency shift at  $80^\circ$  and the optical constants of Si**

Mode order ( $m$ )	ODR frequency shift at $80^\circ$ (%)	Optical constants of Si	
		$n$	$k$
2	6.4	3.63	0.03
3	5.3	3.82	0.014
4	4.2	4.05	0.034
5	3.2	4.33	0.075
6	2.3	4.66	0.14
7	1.5	5.05	0.22
8	1	5.55	0.36

### 3. Theories for MD-layered structures as perfect absorbers

We now provide a theoretical model to discuss the absorption behaviors of the MD-layered structures. The conceptual diagram is schematically illustrated in Fig. 2(a). The amplitudes of the incident (coupled) and reflected (circulated) waves for the free-space (cavity) zone are denoted by  $a_1$  ( $b_2$ ) and  $b_1$  ( $a_2$ ), respectively. The incident field at the coupling section (top mirror layer) is partially reflected and transmitted by a factor of  $r$  (reflectivity) and  $\kappa$  (transmissivity or fractional radiative loss through a top mirror), respectively. The light-absorber interaction can be described by the scattering matrix relation as follows [21]:

$$\begin{bmatrix} b_1 \\ b_2 \end{bmatrix} = \begin{bmatrix} r & -\kappa \\ \kappa^* & r^* \end{bmatrix} \begin{bmatrix} a_1 \\ a_2 \end{bmatrix}. \quad (1)$$

The coupled wave  $b_2$  undergoes a fractional field decay through the lossy structure and thus the circulated wave  $a_2$  is given by

$$a_2 = C e^{i\phi} b_2, \quad (2)$$

where  $C$  and  $\phi$  is the inner circulation amplitude factor and total phase shift per cavity round-trip. Using Eq. (1) and (2), the reflected wave  $b_1$  can be written in the following form:

$$b_1 = \frac{r - C e^{i\phi}}{1 - r^* C e^{i\phi}}. \quad (3)$$

For the convenience of implementing numerical results, we replace the inner circulation factor  $C$  to be  $(1-\alpha^2)^{0.5}$ , where  $\alpha$  represents fractional absorptive loss per round-trip and will be obtained by numerical simulation. There is no transmission through the bottom metal layer, so that the absorptivity can be defined to be  $A = 1 - |b_1|^2$  for unit incidence ( $a_1 = 1$ ). With the relation  $|\kappa|^2 + |r|^2 = 1$  from unitary matrix, the absorptivity  $A$  at resonance can be expressed in terms of the cavity losses as follows:

$$A = 1 - |b_1|^2 = \alpha^2 \kappa^2 \left( \sqrt{(1-\alpha^2)(1-\kappa^2)} - 1 \right)^{-2}. \quad (4)$$

The radiative and absorptive losses arise mainly from the partial transmissions by the top mirror layer ( $\kappa$ ) and the lossy materials ( $\alpha$ ), respectively. When satisfying the critical coupling condition, where  $\kappa$  matches with  $\alpha$  in Eq. (4), it gives complete destructive interference between  $ra_1$  and  $\kappa a_2$ , and then realizes a perfect absorption state ( $A = 1$ ). This design concept has been implemented in the perfect absorbers employing a pair of MD layers [6], optical antennas [22], and thermal emitters [23].

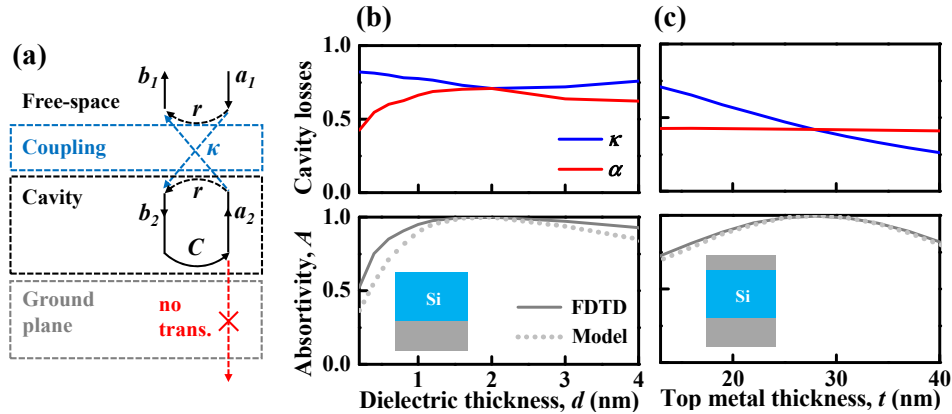


Fig. 2. (a) Theoretical model describing the coupling and absorption procedures of the MD-layered structures. Cavity losses and absorptivity  $A$  under normal incidence for (b) the Si-core double-layer structures ( $t = 0$ ) as a function of dielectric thickness  $d$  and (c) triple-layer structures ( $d = 40$  nm) as a function of the top metal thickness  $t$ . The blue and red solid lines in the upper panels indicate the radiative ( $\kappa$ ) and absorptive ( $\alpha$ ) losses per round-trip, respectively. The absorptivity  $A$  (lower panels) is calculated based on the FDTD method (gray solid lines) and the theoretical model (gray dotted lines).

We perform finite-difference time-domain (FDTD) simulations with the same optical constants used in the TMM calculations to verify the critical coupling concepts. In these



simulations, a fundamental mode ( $m = 0$ ) with a relatively thin dielectric (Si) layer is considered to avoid complexities (the mode number  $m$  indicates the number of field nodes at the dielectric region). A plane-wave source is set to be incident on the top mirror surface for calculating the absorptivity  $A$  at resonance. The in-plane Bloch boundary condition produces the wave vector components corresponding to the incident angles. The cavity quality factor ( $Q$ ) is calculated to determine a total fractional power loss per round-trip ( $2\pi/Q$ ) and then decomposed into its absorptive and radiative components to evaluate  $\alpha$  and  $\kappa$ , respectively. The obtained values of  $\alpha$  and  $\kappa$  are also used for the verification with Eq. (4).

Figures 2(b) and 2(c) present the calculated cavity losses and the absorptivity  $A$  from our theoretical model (Eq. (4)) in comparison with FDTD simulations for the MD double-layer and MDM triple-layer absorbers. For the double-layer structures, the values of  $\kappa$  and  $\alpha$  rely only on the optical constants  $n$ ,  $k$  (depending on  $\lambda$ ) of the dispersive materials and are difficult to control in practice. Although the values of  $n$  and  $k$  can be tuned by introducing free carrier dispersion and absorption, their tuning ranges are limited to below a few percent [24]. For this reason, the resonant wavelength should be properly tuned to obtain  $\kappa = \alpha$  by changing the core dielectric thickness  $d$  as shown in Fig. 2(b). The double-layer absorber with  $d = 2$  nm thickness functions as a nearly perfect absorber at the wavelength of  $\sim 365$  nm. At this point, the value of  $\kappa$  reaches its minimum due to high index contrast. The highest refractive index contrast between the air and the Si material occurs at the wavelength of  $\sim 370$  nm where  $n = \sim 6.83$  and  $k = \sim 2$  according to Palik's data [19]. The extremely thin dielectric thickness  $d$  compared to the resonant wavelength is mainly due to the non-trivial reflection phase shifts (different from 0 or  $\pi$ ) at the interface between the free-space and the lossy dielectric medium, where  $n$  and  $k$  values are comparable to each other [6].

The important advantage of the proposed MDM triple-layer structures is that we can readily manipulate  $\kappa$  regardless of the dielectric core material properties by changing the thickness of the top metal layer,  $t$  (Fig. 2(c)). As  $t$  increases from 0 nm, the resonant modes become more tightly confined within the dielectric core layer ( $r$  increases) and hence  $\kappa$  decreases by the relation  $|\kappa|^2 + |r|^2 = 1$ . In contrast,  $\alpha$  is nearly constant and independent of  $t$ . The parameter  $\kappa$  can thus be manipulated to match with  $\alpha$  at  $t = 28$  nm, where the resonant wavelength is at around 650 nm. At this critical coupling condition ( $\kappa = \alpha = 0.42$ ), the absorptivity calculated from the FDTD method reaches its maximum value of 0.996 (gray solid line). These results are well-consistent with the predictions from the theoretical model (gray dotted line). We also point out that the radiative loss  $\kappa$  varies considerably depending on either the angle of incidence or its polarization state. As an example, the value of  $\kappa$  for an oblique incidence of  $40^\circ$  becomes 0.37 and 0.47 for TE and TM polarization, respectively, and they differ from the normal incidence case ( $\kappa = 0.42$ ).

#### 4. Numerical simulations on multiband perfect absorbers

In the rest of this paper, we primarily focus our discussions on the silicon-cored multiband MDM absorbers with  $d = 300$  nm. Based on the critical coupling concepts, we describe how much absorption (absorptivity  $A$ ) occurs in terms of the incident angle, polarization state, and mode orders  $m$ . To determine the absorptivity  $A$ , we solved the Fresnel coefficients for multilayer systems. Figures 3(a) and 3(b) present the absorption spectra as a function of the top metal thickness  $t$  at the particular incident angles of  $0^\circ$ ,  $40^\circ$ ,  $80^\circ$  (denoted in each map) with different input polarizations. The spectral range is from 400 nm to 1000 nm, where the six resonant modes ( $m = 2\sim 7$ ) dominantly appear.

We first discuss the mode order-dependent absorption characteristics at normal incidence, where the TE and TM modes are equivalent to each other due to the rotational symmetry (left panels in Figs. 3(a) and 3(b)). We note that the lower order modes ( $m = 2, 3, 4$ ) suffer higher  $\kappa$  (over-coupling regime) due to their less confinement within the core layer than the higher order modes (for example,  $m = 5, 6, 7$ ). In this regard, the low-order resonances require thicker  $t$  to reach a critical coupling condition ( $\kappa = \alpha$ ) for better absorption characteristics. On

the contrary, the higher order modes ( $m = 5, 6, 7$ ) lie in the under-coupling regimes ( $\kappa < \alpha$ ) even without the top metal layer. Therefore, as the parameter  $t$  increases, the higher order modes become more under-coupled and exhibit less absorption. With a proper choice of the parameter  $t$ , the proposed structures can act as multiband perfect absorbers (peak  $A > 0.99$ ) whose individual resonances cover a wide range of wavelengths.

The light absorption is also affected by the incident angle and polarization, as can be seen in the center and right panels of Figs. 3(a) and 3(b). As the incident angle varies from  $40^\circ$  to  $80^\circ$ , the optimum  $t$  for the TM polarization increases from 18 to 27.5 nm. In contrast, the optimal absorption point for TE polarization is shifted to smaller  $t$ . This is because the TM (TE) modes have higher (lower)  $\kappa$  for oblique incidence than normal incidence. For the incident angle of  $80^\circ$ , however, the existence of top metal layer merely downgrades the absorption of TE modes, since all of these TE modes fall into the under-coupling regime even without a top metal layer. Our analysis aimed at predicting near-perfect absorption conditions can be useful to further understand the reason why the recently reported triple-layer structures should behave as perfect absorbers [5].

For practical applications, the absorption efficiency of the photoactive dielectric core layer (Si layer) should be considered. For example, the proposed structures with the modes of  $m = 2, 3$  at around 650 and 850 nm wavelengths can be applied to the optical data storage and short-range optical communications. We performed FDTD simulations to evaluate the absorption efficiency in each layer of the MDM structure. When the critical coupling condition is satisfied, the photoactive absorption efficiencies for  $m = 2$  and 3 at normal incidence are estimated to be 0.27 and 0.50, respectively.

Furthermore, we examine how the top metal layer influences the isotropic angular responses for both polarizations. For this purpose, we show the contour plots of the light absorption spectra versus the incident angle for the TE (Fig. 4(a)) and TM modes (Fig. 4(b)) with different  $t$  of 0, 15, 30 nm (denoted in each panel). The maximum extent of the incident angle, defined here as  $\theta_o$ , is  $80^\circ$  for these calculations. We do not consider the case where the incident angle is larger than  $80^\circ$  because of the effect of SPPs at large oblique incident angles.

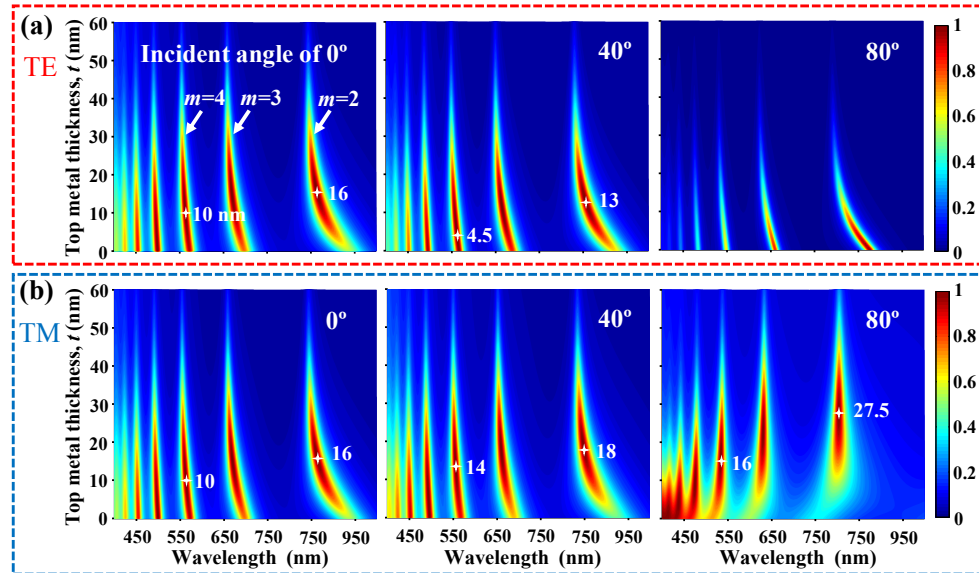


Fig. 3. Calculated (a) TE and (b) TM absorption spectra as a function of top metal thickness  $t$  for the Si-core MDM structure ( $d = 300$  nm) at the incident angle of  $0^\circ$ ,  $40^\circ$ , and  $80^\circ$ . The color bar on the right side of the figure provides color codes for absorptivity. The optimum values ( $t$ ) achieving near-perfect absorption for the RWs ( $m = 2, 4$ ) are displayed (star) in each panel.



As shown in the center panels of Figs. 4(a) and 4(b), the low order modes ( $m = 2, 3$ ) under a proper coupling condition with  $t = 15$  nm maintain highly efficient absorption less sensitive to the incident angle as well as the input polarization. On the other hand, the angular responses at  $t = 0$  and 30 nm exhibit largely unbalanced distribution and sensitively dependent on their polarization. To be noticed, some TM modes ( $t = 15$  nm for  $m = 4, 5$ ) exhibit highly efficient and nearly isotropic responses. However, the corresponding TE modes have relatively weak and non-isotropic responses. In the context of the above results, the thickness of the top metal layer plays a critical role in enhancing the light absorption from the MDM structures. It also controls the dependence on the incident angle and polarization.

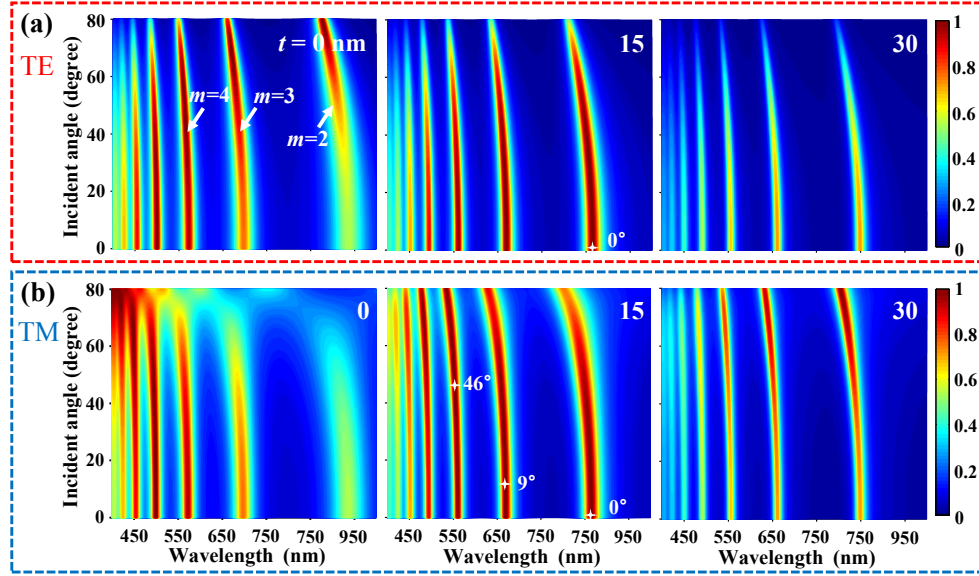


Fig. 4. Calculated (a) TE and (b) TM absorption spectra as a function of the incident angle for the Si-core MDM structures ( $d = 300$  nm) with different  $t$  of 0 nm, 15 nm, and 30 nm. The star symbol in the center panels indicate the critical angles (optimal absorption points).

## 5. Angular response analysis

To further understand the angular absorption behavior discussed in the last section, we define and quantify the angular absorption uniformity and similarity between each polarization. The figure of merit for the highly efficient and angle-independent absorption is the average absorptivity over an incidence angular range, defined here as isotropic factor ( $IF$ )

$$IF_m^{TE(TM)} = \int_{\theta=0}^{\theta_o} A_m^{TE(TM)}(\theta) d\theta / \theta_o, \text{ where } A_m^{TE(TM)}(\theta) \text{ is the angular absorptivity profile for a}$$

given  $m$ -th order TE (TM) mode. Likewise, the similarities and resemblance between the TE and TM responses can be measured by the overlap integral between the TE and TM responses, defined here as cross polarization coupling  $XPC_m = \int_{\theta=0}^{\theta_o} A_m^{TE}(\theta) A_m^{TM}(\theta) d\theta / \theta_o$  for a given mode. Since these quantities account for overall absorption efficiency, the incident light can be perfectly absorbed in all direction irrespective of its input polarization provided that the  $IF$  and  $XPC$  are designed to be close to unity.

The relation between  $IF$  and  $t$  is described in the upper panels of Fig. 5 to identify the exact value of  $t$  permitting the optimal  $IF$  for each resonance ( $m = 2, 3, 4$ ). From these results, the maximum  $IF$  of TE (TM) mode is estimated to be 0.95 (0.97) at  $t$  of 12 nm (20 nm), 0.94 (0.98) at  $t$  of 10 nm (18 nm) and 0.94 (0.99) at  $t$  of 2 nm (14 nm) for  $m = 2, 3$  and 4, respectively. The polar plots of the angular responses for the TM modes under the optimum  $IF$  conditions are shown in the insets within the upper panels of Fig. 5. It is shown that the

maximally absorbed angle of incidence (referred to here as a critical angle) with the perfect absorption ( $A > 0.99$ ) appear near the middle-angle regions and the value of  $A$  is well maintained above 0.9 for all incident angles. Similar behaviors are also observed for the TE modes. The MDM structures can also be designed to improve the  $XPC$  parameter for the given mode order of  $m = 2, 3$ , and 4, as shown in the lower panels of Fig. 5. The high  $XPC$  values of around 0.9 are obtained for  $m = 2, 3$  and 4 with different  $t$  of 16, 14 and 10 nm, respectively, and the angular distributions for both polarizations are similar to each other (insets in the lower panels of Fig. 5). It is worthwhile to note that the  $XPC$  peaks are located in the middle of the  $IF$  peaks and their critical angles appear close to the normal incidence.

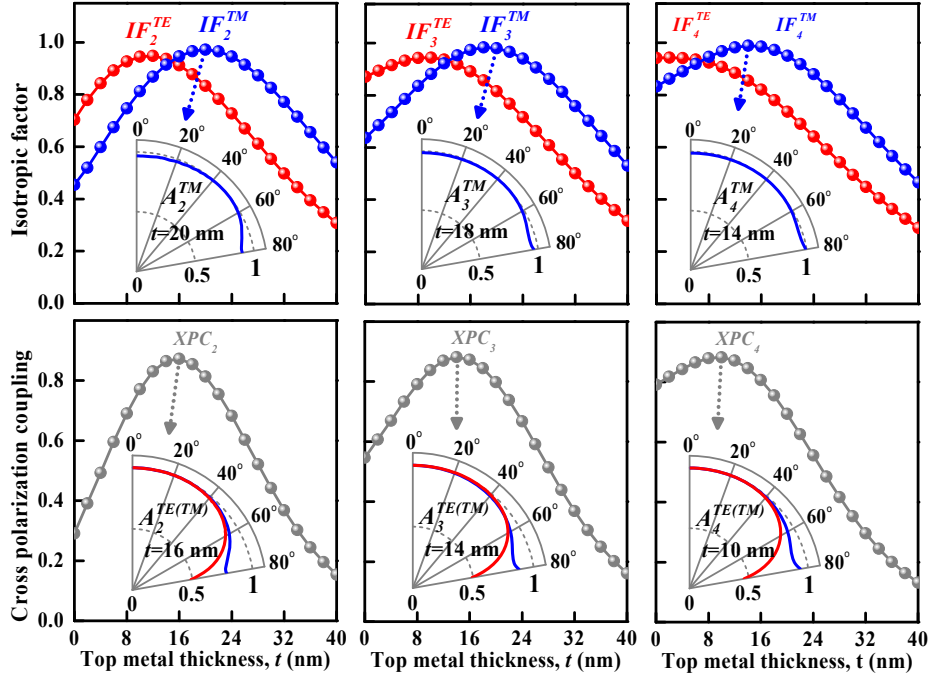


Fig. 5. Isotropic factor ( $IF$ ) for each polarization and cross polarization coupling ( $XPC$ ) of the Si-core MDM structures ( $d = 300$  nm). The  $IF$  (upper panels) and  $XPC$  (lower panels) as a function of the top metal thickness  $t$  are plotted in left, center, and right panels for  $m = 2, 3$ , and 4, respectively. Polar plots are displayed in the insets at each optimal condition. In each panel, the red and blue curves represent the results for the TE and TM modes.

The critical angles (maximally absorbed angle of incidence) and angular responses of each polarization for the case of  $m = 2$  are demonstrated as a function of  $t$  in Figs. 6(a) and 6(b), respectively, to further understand the role of the critical angles on the angular responses. As can be seen in Fig. 6(a), the critical angles vary considerably by modifying  $t$  for both polarizations. As  $t$  increases from 0 to 14 nm, the critical angles decrease from  $80^\circ$  to  $30^\circ$  for the TE modes (red curve in Fig. 6(a)). In contrast, when implementing the thicker top metal layer with  $t$  from 18 to 28 nm, the critical angles of the TM modes increase from  $32^\circ$  to  $80^\circ$ . For the range of  $t = 0 \sim 14$  nm ( $t = 18 \sim 28$  nm), the TM (TE) modes exhibit relatively less efficient and more directional operation (e.g.  $t = 8$  nm for TM and  $t = 28$  nm for TE in Fig. 6(b)). The reason behind this opposite trend is that the radiation losses ( $\kappa$ ) of the TE and TM modes oppositely behave with respect to  $\theta$  at a given  $t$  (see Fig. 3).

As an example, let us consider the most isotropic responses ( $IF \sim 1$ ) at  $t = 12$  and 20 nm for the TE and TM mode, respectively (Fig. 6(b)). At each point, the critical angle is estimated to be  $\sim 45^\circ$ . In the region ranging from  $0^\circ$  to  $\sim 45^\circ$ , the TE modes are over-coupled ( $\kappa > \alpha$ ), whereas the TM modes are under-coupled ( $\kappa < \alpha$ ). Therefore, if we decrease  $\kappa$  (increase  $t$  from

12 nm) for TE and increase  $\kappa$  (decrease  $t$  from 20 nm) for TM, the critical angles of the TE and TM modes become smaller than  $\sim 45^\circ$ . Under an intermediate value of  $t = 16$  nm, the critical angles of both polarizations are eventually close to each other (normal incidence) and their angular responses also become highly efficient.

In this section, we found that the critical angles of each resonance can be properly designed to either enhance the uniformity of the angular responses or reduce the polarization dependence by manipulating the top metal thickness  $t$ . The operation principles of the MDM absorbing structures studied here can shed light on the mechanisms underlying the optical angular responses of more general electromagnetic wave absorbers such as planar and perforated structures.

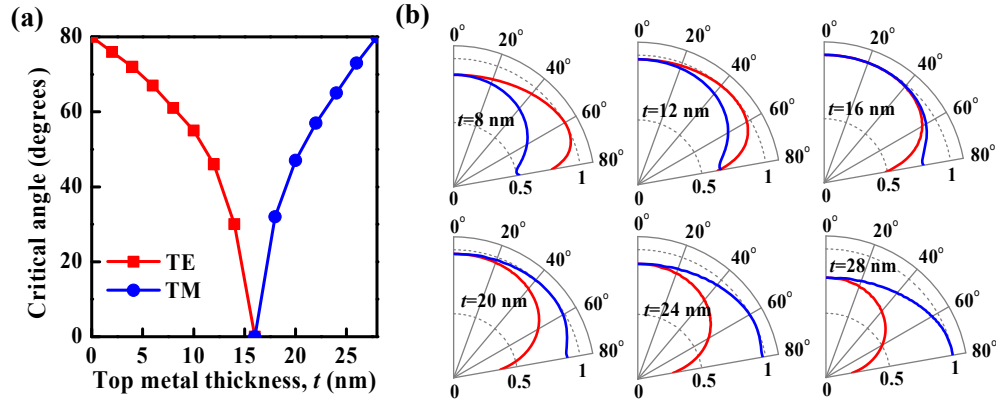


Fig. 6. (a) Critical angles of the second-order TE and TM resonances ( $m = 2$ ) for the Si-cored MDM structures ( $d = 300$  nm) when varying the top metal thickness  $t$  from 0 to 28 nm. The red and blue lines indicate TE and TM modes, respectively. (b) Angular absorptivity profiles of each polarization for six different top metal thicknesses: 8, 12, 16, 20, 24, and 28 nm.

## 6. Conclusion

We have demonstrated that a planar metal-dielectric layered structure can be used for a multiband absorber with omnidirectional and polarization-insensitive characteristics. Due to the slower group velocities from an optically dense dielectric medium, the cavity resonant frequencies can remain nearly identical in all receiving-directions regardless of the input polarization. The light absorption behaviors against the angle of incidence and the polarization state are elucidated using an analogy with the well-known critical coupling concepts. We establish a theoretical model with numerical verification to reveal the role of the thin top metal layer on the highly efficient and near-isotropic absorption features. The operation mechanisms for the suggested wide-angle perfect absorption can be extended to further understand the angular responses of various kinds of light absorbers including simple planar structures as well as perforated plasmonic and metamaterial devices. The proposed metal-dielectric absorbing structures can pave the way for numerous applications such as photo-detectors, optical filters and photovoltaic cells due to their structural simplicity and functional versatility.

## Acknowledgments

This research was supported by the National Research Foundation of Korea (NRF) grant funded by the Korean Government (MEST) (2008-0062256, 2010-0002845) and the Center for Integrated Smart Sensors funded by the Ministry of Science, ICT & Future Planning as Global Frontier Project (CISS-2012M3A6A6054191).